The Luminosity Function for White Dwarfs in the SuperCOSMOS Sky Survey.

N. R. Rowell[1]★, N. C. Hambly[1], P. Bergeron[2]

[1] Institute for Astronomy, University of Edinburgh, Blackford Hill, Edinburgh EH9 3HJ
[2] Département de Physique, Université de Montréal, C.P. 6128, Succ. Centre-Ville, Montréal, Québec H3C 3J7, Canada

E-mail: ★ nr@roe.ac.uk
[2] bergeron@astro.umontreal.ca

Abstract. We present the techniques and early results of our program to measure the luminosity function for White Dwarfs in the SuperCOSMOS Sky Survey. Our survey covers over three quarters of the sky to a mean depth of $I \sim 19.2$, and finds $\sim 9,500$ Galactic disk WD candidates on applying a conservative lower tangential velocity cut of 30kms^{-1}. Novel techniques introduced in this survey include allowing the lower proper motion limit to vary according to apparent magnitude, fully exploiting the accuracy of proper motion measurements to increase the sample size. Our luminosity function shows good agreement with that measured in similar works. We find a pronounced drop in the local number density of WDs at a $M_{bol} \sim 15.75$, and an inflexion in the luminosity function at $M_{bol} \sim 12$.

1. Introduction

The potential use of White Dwarfs (WDs) as chronometers has long been recognised. The relative accuracy of stellar age estimates based on up-to-date models, combined with the long evolutionary timescales of WDs and their abundance in most Galactic systems, means this approach has been used to age a wide variety of stellar configurations. These include WD - subdwarf binaries (Monteiro et al. 2006), single burst populations such as globular and open clusters (Hansen et al. 2007; von Hippel & Gilmore 2000, Jeffery et al. 2007), and continuous populations such as the Galactic disk (Winget et al. 1987, Oswalt et al. 1995, Leggett et al. 1998). The standard tool used for this technique is the luminosity function (LF) for WDs, which contains information on both the absolute age and the star formation history of a stellar system. The star formation history is essentially imprinted on the entire LF, and authors working on parametric forms for the LF (eg. Noh & Scalo 1990) predict bumps and inflexions corresponding to changes in the rate of star production in the past. The absolute age is constrained by the marked downturn in the LF at faint magnitudes, where the cooling ages of WDs converge on that of the population as a whole.

Modern surveys that apply this to the Galactic disk have suffered from small observational samples of faint WDs at the LF turning point. This is confounded by the fact that the atmospheric physics of such 'ultracool' WDs is currently poorly understood, with only a handful of stars extensively studied (eg Bergeron & Leggett 2002). The largest LF measurement currently published is that of Harris et al. (2006), using a sample of 6000 WDs selected from a combination

of the SDSS and USNO-B. The presence of only 4 stars beyond the turning point precludes any accurate constraint on the LF at these magnitudes.

We are working on a program to measure the WDLF by exploiting data from the all-sky SuperCOSMOS Sky Survey (SSS). Sensitive proper motion detection combined with accurate photometry over wide angles enables large samples of WDs to be catalogued using reduced proper motion methods. In section 2 we outline the SSS, and go on to descibe our survey procedures in sections 3, 4 and 5. We present our LF in section 6, and discuss the limitations and possible future refinements in section 7.

2. The Data

The SuperCOSMOS Sky Survey was compiled by digitizing several generations of photographic Schmidt plate surveys. The photographic source material includes the POSS-I and POSS-II surveys in the northern hemisphere, and a combination of ESO and SERC surveys in the south. Over 1700 fields are required to cover the entire sky, with each field being observed in four photographic bands $B_J R_{59F} I_N$ and $R_{103aE/63F}$ in the north/south respectively. Only $B_J R_{59F}$ and I_N are normally used for photometry, $R_{103aE/63F}$ being generally of poorer quality and very similar in response to R_{59F}. $R_{103aE/63F}$ is used to provide an early epoch for improved astrometric solutions in each field. The subscripts refer to particular filter/emulsion combinations, and will be dropped throughout the rest of this paper. We will sometimes refer to $R_{103aE/63F}$ and R_{59F} as first- and second-epoch R respectively. Due to reasons outlined in section 4.1.1, we restrict our analysis to objects detected at all four epochs. The survey data is housed in relational databases available online at `http://surveys.roe.ac.uk/ssa/`. An introduction to the SSS and further technical details can be found in Hambly et al. 2001a. We avoid the Galactic plane by 10° and the centre by 20°. These regions are heavily affected by blending and poor photometric calibration due to differential extinction within the field. We also reject six fields centred on the Magellanic clouds for the same reasons. This gives a total sky coverage of 10.2 sr, or about 80% of the sky. Taking into account the regions lost around bright stars due to diffraction spikes and scattered light haloes, the total survey area is 9.4 sr, or just over 75% of the sky.

3. Sample Selection

3.1. Image morphology criteria

The SuperCOSMOS Image Analysis Mode software measures 32 parameters for each object detection, some of which we restrict in order to ensure our final WD catalogue only contains objects with reliable, high quality images. We only accept objects with the *deblending flag* set to zero, meaning no image fragmentation has been detected. The *quality number* is an integer indicating situations encountered during image analysis, such as proximity to a bright star or plate boundary, and is set such that increasingly severe circumstances are assigned higher values. We restrict this parameter to values less than 128. The *profile classification statistic* η gives a magnitude-independent measure of the 'stellarity' of an image, by quantifying the deviation of the radial profile slope from that of the mean stellar template. It is scaled to a zero mean, unit variance Gaussian distribution. Objects with $|\eta| > 4\sigma$ are rejected.

Previous studies utilising digitized Schmidt plate data have placed cuts on the ellipticities of images, in order to limit contamination by faint galaxies and noise. However, we have found that the ellipticities measured by SuperCOSMOS are extremely noisy at intermediate to faint magnitudes, and that any intuitively sensible cut will result in a seriously incomplete sample of stars. This may be due in part to the eight-fold nearest neighbour pixel connectivity employed by the SuperCOSMOS image analysis software. We have decided to ignore this parameter.

3.2. Contamination in north due to repeated photographic copying

The northern half of the SSS data was digitized from photographic copies of POSS-I and POSS-II survey originals. Unfortunately, this seems to have degraded the quality of the data, resulting in erroneous astrometric fits for a fraction of objects. This may be due to the photographic copying process rendering blended objects harder to detect. Certainly, the distribution of the astrometric residuals for affected objects deviates significantly from the expected χ^2 form, indicating that something is going wrong with the centroiding. This problem first became obvious when we started to analyse the reduced proper motion (RPM) diagram for the northern hemisphere (see section 5), and noticed an extended population of objects at high values of RPM, in approximately the same region as cool WDs. This is what is expected if the proper motions of objects no longer correlate with distance - essentially, stars with bad proper motions are scattered from their usual locii and any discrimination between distinct Galactic and stellar components is lost. The main consequence for this work is that the highly numerous disk main sequence stars tend to scatter into the WD region, completely swamping the cool WD locus. Unfortunately, this contamination cannot adequately be removed by simply applying judicious selection cuts on the image parameters, and we have been forced to devise a new statistic to identify these objects. This statistic is calculated using the known distributions of χ^2 (astrometric fit residuals) and η for both reliable and unreliable objects. The main result is that bad objects are successfully removed by placing a selection cut on this new statistic, and that a certain fraction of good objects are also removed. This fraction can be precisely measured and corrected for in later analysis, given that this statistic is independent of magnitude, colour and proper motion.

4. Survey Limits

4.1. Proper Motion

The upper limit on proper motions is set to $0\farcs18$ yr^{-1} for the entire survey. This arises from the mean epoch spread and reliable pairing radius between consecutive observations in each field. This limit is not so important for producing large stellar catalogues, due to the lower probability of stars having such motions. Note, however, that nearby ultracool WDs and halo stars are expected to show larger motions. To produce a large sample of stars, we reduce the lower proper motion limit as far as possible while maintaining a 5σ proper motion detection threshold on all objects. This level has been chosen to limit observational scatter in the RPM diagram. Our lower limit is thus dictated by the proper motion errors, which in general differ from field to field due to varying time baselines and plate quality, and within individual fields are a function of apparent magnitude, due mostly to centroiding precision as detailed in section 2.2.5 of Hambly et al 2001c. It is natural therefore to allow our lower proper motion limit to vary from field to field, and to make it a function of apparent magnitude within each field. In general, there is no analytic form for the distribution of proper motion errors with apparent magnitude, and a numerical solution has to be found.

4.1.1. Proper motion limit as a function of apparent magnitude For every survey field, we plot the proper motion uncertainty σ_μ against B for all objects. Many fields share the same general form for this distribution, in particular a minimum of $\sigma_\mu \sim 5$ mas yr^{-1} at around $B \sim 17$, rising to considerably larger errors at brighter and fainter magnitudes. Objects detected on only three plates show a similar distribution offset to larger σ_μ by up to $0\farcs04$ yr^{-1}. Rather than attempting to define a separate lower proper motion limit for these objects, we simply discard them. We wish to find the upper boundary of this distribution, denoted $\sigma_\mu^{\rm upper}(B)$. We may then define our 5σ-threshold lower proper motion limit at every magnitude by simply multiplying this function by 5. $\sigma_\mu^{\rm upper}(B)$ is estimated by first binning objects according to magnitude, interactively so that each bin contains 100 points, which allows reasonable estimation of $\sigma_\mu^{\rm upper}(B)$ at the extremes where objects are of low density. This results in N bins, where $N = N_{\rm objects}/100$

and is typically of the order of 100. Each of the N points $\sigma_\mu^{\rm upper}(B_N)$ is then defined by the largest σ_μ at the mean B value in each bin, after rejecting the top 3% of points as outliers. The set of points $\sigma_\mu^{\rm upper}(B_N)$ shows considerable noise on small scales, and is processed through one stage of smoothing to remove this. A Savitzky-Golay filtering technique is used (Savitzky & Golay 1964), generalized to allow for non-regular data. This results in a final set of N points $\sigma_\mu^{\rm upper}(B_N)$, which are interpolated linearly to define $\sigma_\mu^{\rm upper}(B)$ at all magnitudes. Figure 1 shows an example of the proper motion error distribution and $\sigma_\mu^{\rm upper}(B)$ for one field.

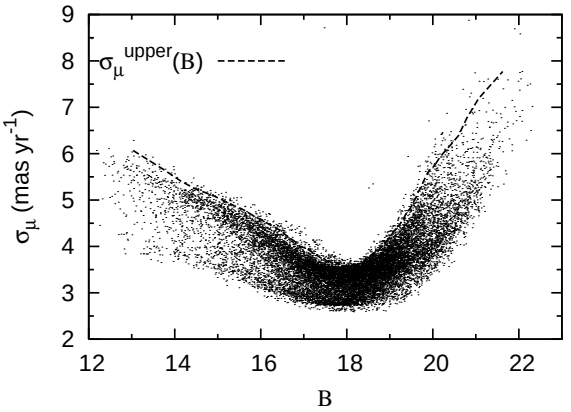

Figure 1: Proper motion error distribution for northern field 12, with the upper boundary set by $\sigma_\mu^{\rm upper}(B)$.

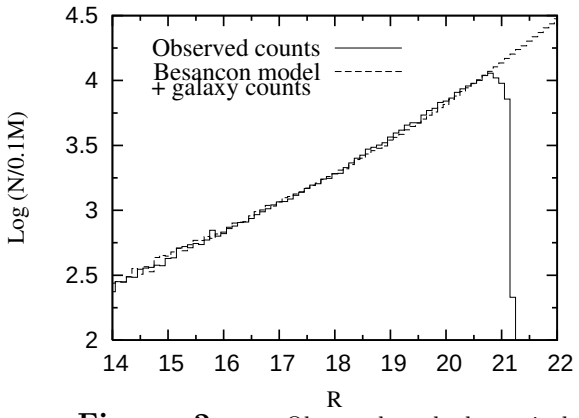

Figure 2: Observed and theoretical number count histograms for SERC-R survey field 149.

4.2. Magnitude

The magnitude completeness of catalogues derived from Schmidt plates has been analysed extensively in the literature. We follow a similar approach to Tinney, Reid and Mould (1993), except that with nearly 8000 Schmidt plates in 1700 fields it is unfeasible to model the differential stellar and galactic number counts in each. We proceed by assuming that within each of the eight photographic surveys compiled into the SSS the completeness of each plate is an identical function of the plate detection limit. This allows for the considerable variation in depth of plates within each survey. We estimate the *completeness function* for each survey, using a subset of five fields chosen at high Galactic latitude, in order to reduce the effects of image crowding and interstellar extinction. The completeness function is defined to be the fraction of objects recovered as a function of apparent magnitude, and relies on an estimate of the intrinsic stellar and galactic number counts in each field. Figure 2 shows the typical number count histograms for observed and modelled data in one field.

4.2.1. Theoretical source counts Intrinsic stellar number counts are modelled using the Besancon Galaxy model (Robin et al. 2003). These will generally be different in each field due to different lines of sight through the Galaxy. Conversely, galaxy number counts are assumed to be isotropic, with the large ($\sim 6^\circ \times 6^\circ$) fields smoothing out any small scale structure. Suitable empirical counts have been published by many authors (eg Jones et al. 2001), and in this study we use those compiled by the Durham Cosmology Group[1]. In log-number space the galaxy counts are well fitted by straight lines in each band over the range of interest.

4.2.2. Completeness of digitized Schmidt plates as a function of plate depth The completeness function in each field is given by $\mathcal{C}(m) = N_{\rm obs}(m)/N_{\rm intrinsic}(m)$. For each survey we obtain five measures of $\mathcal{C}(m)$, which are individually shifted according to the plate depth then averaged

[1] Available online at `http://star-www.dur.ac.uk/~nm/pubhtml/counts/counts.html`

to obtain $\overline{\mathcal{C}}(m')$, where m' is magnitudes above the plate limit. Uncertainties are assigned from the sample variance of the individual measures. The resulting eight functions are used to define dynamic magnitude limits for the remaining fields in each survey. One such function is presented in figure 3. The offset from the plate limit chosen as the completeness limit (m'_{lim}) for each survey is given in table 1, along with the corresponding mean magnitude limits for each band.

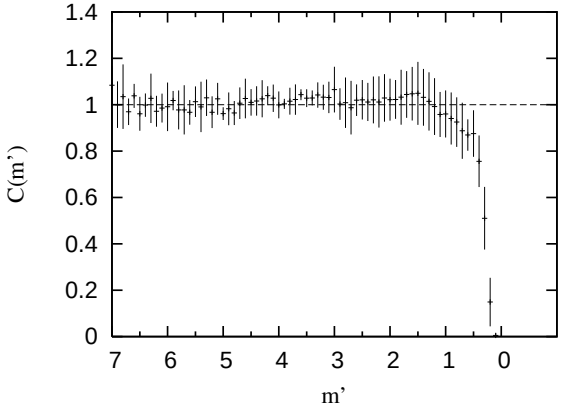

Figure 3: Mean completeness function for survey ESO-R. m' refers to magnitudes above the plate limit; in this example $m'_{lim} = 0.6$.

Survey	m'_{lim}	Mean depth
Northern hemisphere:		
POSSI-E	0.8	20.2
POSSII-B	0.6	22.0
POSSII-R	0.7	20.5
POSSII-I	0.6	19.4
Southern hemisphere:		
ESO-R	0.6	20.3
SERC-J	0.5	22.2
SERC-R	0.5	20.5
SERC-I	0.6	19.0

Table 1: Completeness limit offsets and mean depth of surveys.

5. Methods

5.1. Reduced proper motion

The *reduced proper motion* statistic $H_m = m + 5\log(\mu) + 5$ uses the correlation between proper motion and distance to estimate the absolute magnitude of nearby stars, and is commonly employed for identifying extremely sub-luminous WDs in proper motion surveys. The fact that H_m can be expressed in quantities intrinsic to the star $H_m = M + 5\log(V_{tan}) - 3.379$ suggests that we can use stellar and kinematic models to predict the range of H_m for WDs of various colour and velocity. This allows us to perform rigorous selections on H_m to produce well defined catalogues of WD candidates. This is done in the H_m-colour plane, where an appropriate colour-magnitude relation can be used to find the regions inhabited by WDs of various tangential velocity. Figure 4 shows the reduced proper motion diagram (RPMD) for our objects. This is topologically similar to the HR diagram. Cooling tracks for WDs with hydrogen and helium atmospheres and a range of V_{tan} are plotted. WDs of larger tangential velocity are located below these lines, and we select objects from below the DA track as our WD candidates.

5.1.1. Tangential velocity cut Cool WDs of low velocity share identical values of H_m with subdwarfs in the high velocity tail of the halo, so these two populations overlap to some extent in the RPMD. Contamination by subdwarfs can be reduced by applying a minimum tangential velocity threshold to the kinematic selection of WDs. This essentially selects WD candidates from regions more widely separated from the subdwarf locus. The fraction of WDs that fall below the chosen V_{tan} threshold can be corrected for by including a 'discovery fraction'. This is calculated by projecting the WD velocity ellipsoid onto the sky, and integrating the resulting V_{tan} distribution over the range of allowed velocities, according to the prescription of Murray (1983). As each line of sight sees a slightly different projection of the velocity ellipsoid, this has to be done separately for each survey field. We assume the velocity ellipsoid for disk WDs matches that of local dM stars measured by Reid et al 1995, and set $\sigma_{\mathrm{u,v,w}} = (43,31,25)$ kms^{-1} with an asymmetric drift of -22 kms^{-1} relative to the local standard of rest. The discovery fraction has a mean value of 0.85 (0.69) (0.52) for $V_{tan} > 20(30)(40)$kms^{-1}.

5.2. Photometric parallaxes

Photometric distances and temperatures are obtained by fitting the two SSS colours using the model atmospheres and cooling sequences described in Bergeron et al. (2001) and references therein (see also `http://www.astro.umontreal.ca/~bergeron/CoolingModels`), provided in the SuperCOSMOS passbands and interpolated at 10K intervals.

The appropriate two-colour diagram and model tracks are presented in figure 6. We use a simple variance-weighted least-squares fitting procedure, and reject objects with $\chi^2 > 5$. Such objects are mostly unresolved binaries, as detailed in section 5.2.2. With only one degree of freedom we cannot measure the gravity or atmosphere type of each star, so we assume $\log(g) = 8$ for all stars and fit both hydrogen (DA) and helium (DB) atmospheres. Over- and under-massive WDs exist in roughly equal proportion, and fitting them with normal-mass atmospheres has opposite effects and so should (roughly) cancel out. We make no correction for reddening, as we expect the effect to be very small due to the proximity of our stars.

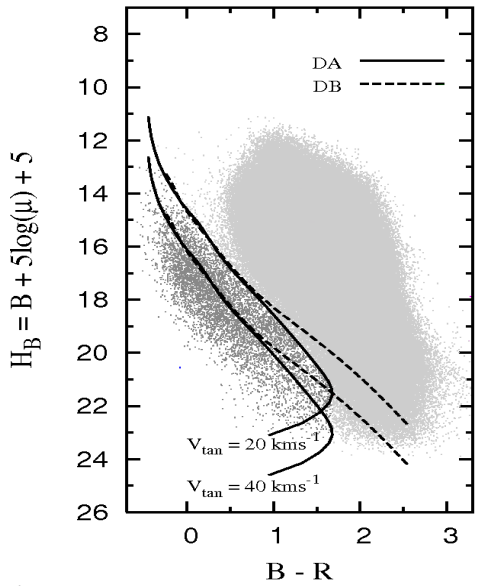

Figure 4: RPMD for stars in SSS. Light grey points are subdwarfs and disk main sequence stars, dark grey points are stars selected as WD candidates.

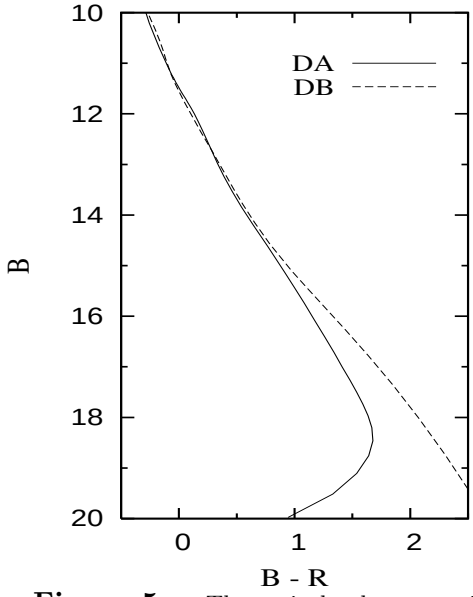

Figure 5: Theoretical colour-magnitude relations for hydrogen-rich (DA) and helium-rich (DB) WDs, assuming a normal surface gravity of $\log(g) = 8$.

5.2.1. WD atmosphere types We allow WD candidates to contribute to the LF as both hydrogen and helium atmosphere WDs, with a weight for each type set according to the observed stellar abundances. For WDs bluer than $B - R \sim 1$, corresponding to $T_{eff} \gtrsim 5250$K, the particular choice of atmosphere has little effect on the fitted luminosity, so we simply assume all stars are hydrogen types. At lower effective temperatures helium atmosphere stars are more luminous, by around 1 mag at $B - R \sim 1.5$ (see figure 5), and we therefore expect helium WDs to be over-represented at the reddest colours. We shift the weight in favour of helium WDs in this range, and set it according to the fitted hydrogen atmosphere absolute magnitude. The values used are given in table 2.

5.2.2. WD+dM binaries WDs with unresolved cool companions will tend to scatter out of the WD locus in the colour-colour plane, due to the companion star contributing flux to the I band. Harris et al. (2006) include these objects in their survey by accepting only the bluest bands, however with only two colours we cannot do this and so must reject these objects. This to some

extent represents an incompleteness in our survey, as around 10% of WD candidates are rejected in this way.

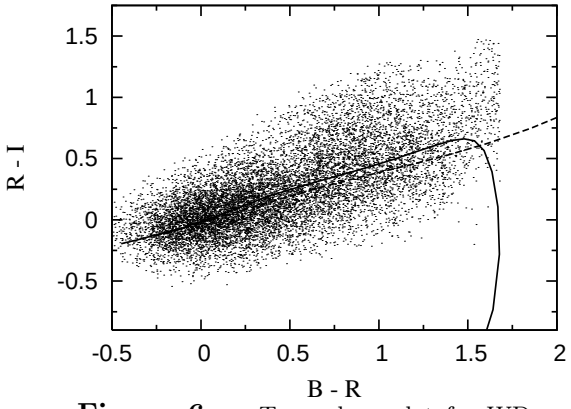

Figure 6: Two-colour plot for WD candidates and synthetic WD models. The dashed line is for helium-rich DB models, the solid line is for hydrogen-rich DAs.

$M_{\rm bol,\ H}$	$\mathcal{W}_{\rm H}$	$\mathcal{W}_{\rm He}$
< 15.2	1.0	0
$15.2 \rightarrow 15.5$	0.5	0.5
$15.5 \rightarrow 16.0$	0.2	0.8
> 16.0	0	1.0

Table 2: Weights assigned to hydrogen and helium atmosphere WDs.

6. Luminosity function methods

6.1. The generalized V_{max} technique

The spatial density of objects retrieved in a survey with both magnitude and proper motion limits can be most readily obtained using Schmidt's $1/V_{max}$ method. This involves summing the inverse of the *maximum* volume in which each object could have been observed, given it's absolute magnitude and tangential velocity, and the survey limits. This method has since been generalised to non-uniformly distributed populations, in particular to allow for the exponential density profile of the Galactic disk. V_{max} is obtained by integrating the density law along the line of sight to the star, over the distance range in which the star passes the survey selection criteria. Errors are assigned to each luminosity bin by assuming Poisson statistics.

6.1.1. V_{max} with dynamic proper motion limits A problem arises when the proper motion limit is allowed to vary with apparent magnitude in a non-analytic way. The distances d_{min} and d_{max} at which the star's proper motion crosses the survey limits can no longer be calculated analytically, and so this integral is evaluated in the following manner. The limiting distances due to the magnitude limits are calculated as normal, then the integral is evaluated numerically between these limits in steps of finite size. At each distance step, the star's proper motion is calculated and compared to the limits appropriate for the new apparent magnitude, and if the star is within the limits then the volume associated with this step is added to the integral. The final stage is to select an appropriate step size for this calculation. We have chosen to use steps of constant *generalized volume*, taking into account the disk density profile. This ensures that each step makes an identical contribution to the sum. Note that calculating the distance interval necessary to keep the generalized volume of each step constant is also non-trivial, and leads ultimately to a transcendental equation that must be solved numerically.

6.2. The White Dwarf luminosity function

The LF derived for the 9480 WDs with $V_{tan} > 30\mathrm{kms}^{-1}$ is presented in figure 7. A scaleheight of 250pc has been assumed for the density profile, to allow comparison with other works. The LF is remarkably featureless on the rising side, apart from a slight inflexion at $M_{bol} \sim 12$. The faint end shows a drop in density at $M_{bol} = 15.75$, in agreement with that reported by other authors. Integrating the LF gives a total WD number density in the solar neighbourhood

of $2.3 \times 10^{-3}\mathrm{pc}^{-3}$. $\langle \frac{V}{V_{max}} \rangle = 0.505 \pm 0.003$ for this survey, somewhat larger than that for a complete survey ($\langle \frac{V}{V_{max}} \rangle = 0.5$) but it should be noted that the assumed scaleheight affects this calculation, and increasing it to 350pc results in $\langle \frac{V}{V_{max}} \rangle = 0.498 \pm 0.003$.

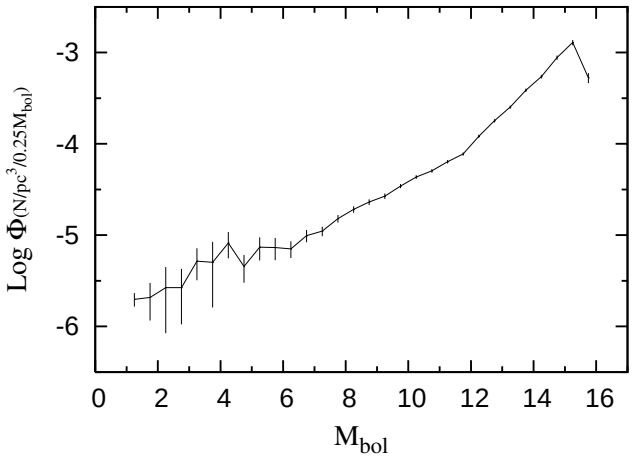

Figure 7. LF for WDs with $V_{tan} > 30\mathrm{kms}^{-1}$.

7. Future Work

Older stars are expected to have larger scaleheights due to kinematic heating, and V_{max} will be underestimated for these objects by assuming a value of 250pc. We intend to improve our LF by measuring the variation in scaleheight with M_{bol} for our objects. Optical spectra have been obtained for a subsample of WD candidates, which we will use to assess the reliability of our method and contamination from non- degenerate stars. We also have a high proper motion catalogue of SSS objects with motions in the range $0\farcs18 < \mu < 10\farcs0$ yr^{-1}, which contains most of the interesting ultracool WDs featured in the literature. Including this will push our disk LF to fainter magnitudes, and will also possibly provide enough halo WD candidates to measure a LF for this component.

References

Bergeron P and Leggett S K 2002 *ApJ* **580**:1070-1076
Bergeron P, Leggett S K and Ruiz MT 2001 *ApJ Suppl.* **133**:413-449
Hambly N C *et al* 2001a *MNRAS* **326**:1279-1294
Hambly N C, Davenhall A C, Irwin M J and MacGillivray H T 2001c *MNRAS* **326**:1315-1327
Hansen, B *et al* 2007 *ApJ* **671**:380-401
Harris H C *et al* 2006 *AJ* **131**:571-581
von Hippel T and Gilmore G 2000 *AJ* **120**:1384-1395
Jeffery E, von Hippel T, Jefferys W, Winget D, Stein N and DeGennaro S 2007 *ApJ* **658**:391-395
Jones L R, Fong R, Shanks T, Ellis R S and Peterson B A 1991 *MNRAS* **249**:481-497
Leggett S K, Ruiz M T and Bergeron P 1998 *ApJ* **497**:294-302
Monteiro H, Jao W C, Henry T, Subasavage J and Beaulieu T 2006 *ApJ* **638**:446-453
Murray C A 1983 *Vectorial Astrometry* 284-287
Noh H and Scalo J 1990 *ApJ* **352**:605-614
Oswalt T, Smith J, Wood M and Hintzen P 1995 *Nat.* **382**:692-694
Reid I N, Hawley S L and Gizis J E 1995 *AJ* **110**:1838-1859
Robin A C, Reylé C, Derriére S and Picaud S 2003 *A & A* **409**:523-540
Savitzky A and Golay M 1964 *Analytical Chemistry* **36**:1627-1639
Tinney C G, Reid I N and Mould J R 1993 *ApJ* **414**:254-278
Winget D, Hansen C, Liebert J, Van Horn H, Fontaine G, Nather R, Kepler S and Lamb D 1987 *ApJ* **315**:L77-L81